JGR Solid Earth

RESEARCH ARTICLE
10.1029/2021JB023718

Special Section:
Heterogeneity, anisotropy and scale-dependency: Keys to understand Earth composition, structure and behavior

Ultralow Melting of Iron Nitrides and the Fe–N–C System at High Pressure

HPSTAR 1403-2022

Chaojia Lv[1] and **Jin Liu**[1,2]

[1]Center for High Pressure Science and Technology Advanced Research, Beijing, China, [2]CAS, Center for Excellence in Deep Earth Science, Guangzhou, China

Abstract Iron nitrides and carbonitrides are the two primary hosts of deep nitrogen in the Earth's interior; hence, the storage and circulation of deep nitrogen can be largely controlled by the melting behavior of iron nitrides and the Fe–N–C system. In this study, the melting temperatures of these minerals were determined individually and jointly using the new diagnostics of electrical resistance jump up to 80 GPa in laser-heated diamond-anvil cells. The solidus curves of these samples are extremely low at mantle pressures, and are marginally affected by the iron spin transition, nitrogen concentration, and carbon incorporation, suggesting that nitrogen-rich metallic liquids likely exist at depths of <1,500 km in the present-day mantle. Meanwhile, our Raman spectra are indicative of N_2 degassing out of iron nitride liquids at <12 GPa. These results suggest that low-pressure N_2 degassing in the proto-Earth coupled with nitrogen-rich liquids hidden in present-day lower mantle play important roles in the redistribution of deep nitrogen through geologic time and space.

Plain Language Summary Compared to carbon, nitrogen is relatively depleted in the crust and mantle, leading to dramatically higher C/N ratios in the bulk silicate Earth with respect to the carbonaceous chondrites, that is, the so-called "missing nitrogen" mystery. Recent studies suggest carbon behaves more siderophile than nitrogen under core conditions; accordingly, more carbon could have entered the core with respect to nitrogen, which only can aggravate the "missing nitrogen" mystery by greatly decreasing the C/N ratio in silicates. Meanwhile, atmospheric loss of primordial nitrogen is insufficient to account for the high C/N ratio due to small difference in the solubility of carbon and nitrogen in magma oceans. Here we investigate the high-pressure melting temperature of iron nitrides and carbides, and find iron nitrides would melt in the present-day mantle at depths of less than 1,500 km. Additionally, we observed N_2 generation out of the Fe–N liquids at relatively low pressures. The extremely low melting temperatures of the Fe–N–C system as well as low-pressure N_2 degassing of the Fe–N liquids may contribute to the redistribution of deep/primitive nitrogen through time and space. Both processes can provide a better understanding of Earth's 'missing nitrogen' mystery.

Key Points:

- The melting behavior of iron nitrides and carbides was investigated to 80 GPa using the novel method of electrical resistance jump
- Iron nitrides have extremely low melting temperatures, which are barely affected by nitrogen content and carbon incorporation
- Low-pressure degassing and high-pressure N-rich metallic liquids may play important roles in the deep nitrogen cycling in the mantle

Correspondence to:
J. Liu,
jin.liu@hpstar.ac.cn

Citation:
Lv, C., & Liu, J. (2022). Ultralow melting of iron nitrides and the Fe-N-C system at high pressure. *Journal of Geophysical Research: Solid Earth*, *127*, e2021JB023718. https://doi.org/10.1029/2021JB023718

Received 27 NOV 2021
Accepted 8 FEB 2022

1. Introduction

Nitrogen is not only crucial for organisms, but also an important tracer for the formation and evolution of terrestrial planets. CI chondrite meteorites were previously thought to represent the bulk composition of our planet; considerable amounts of nitrogen up to 5,000 ppm might have been stored on Earth (Adler & Williams, 2005; Sugiura, 1998). Recent studies suggest the bulk Earth accreted from 70% to 90% reduced enstatite chondrites followed by 10%–30% oxidized CI carbonaceous chondrites, and both chondrites could deliver excess nitrogen to the Earth (Dauphas, 2017; Grewal et al., 2019). However, the abundance of nitrogen in the bulk silicate Earth (BSE) is commonly assessed to be 0.84–33 ppm (Goldblatt et al., 2009; Jacobs et al., 1995; Marty, 2012; Yoshioka et al., 2018; Zhang & Yin, 2012). Furthermore, as the seventh most abundant element in the Solar System, nitrogen is relatively depleted in the BSE with respect to carbon and other volatiles (Bergin et al., 2015; Marty, 2012; Speelmanns et al., 2019). A recent estimate of the C/N ratio for the BSE is 49.0 ± 9.3 (Bergin et al., 2015), which is much higher than the CI carbonaceous chondrites (17.0 ± 3.0) (Alexander et al., 2013), enstatite chondrites (13.7 ± 12.1) (Grady & Wright, 2003), and the interstellar medium gas and dust (Parvathi et al., 2012). Such a paradox has conventionally been called as the "missing nitrogen" mystery.

Nitrogen depletion in the BSE has been mainly ascribed to metallic core sequestration and atmospheric escape (Bergin et al., 2015; Dalou et al., 2017; Hirschmann, 2016; Sakuraba et al., 2021). More recent metal-silicate partitioning experiments, however, revealed that nitrogen is weakly lithophile to moderately siderophile at the

pressure (P), temperature (T), and oxygen fugacity conditions relevant to core formation (Dalou et al., 2017; Dalou et al., 2019; Li et al., 2016; Speelmanns et al., 2019). Given that carbon is much more siderophile than nitrogen, core formation would reduce the C/N ratio of the BSE, running counter to the current estimated values of ~49.0 (Dalou et al., 2017). On the other hand, depletion of volatiles would happen after the dissipation of nebular disk via photo-evaporation, hydrodynamic escape, and the dominant atmospheric escape caused by impacts (Schlichting & Mukhopadhyay, 2018). In the equilibrium system between the terrestrial magma ocean and overlying atmosphere, the partition of volatiles is controlled by solubility constants (Hirschmann, 2016; Tucker & Mukhopadhyay, 2014). Interestingly, atmospheric escape was recently found insufficient for the over-chondritic C/N ratio as revealed by the solubility behavior of carbon and nitrogen at high P-T conditions (Hirschmann, 2016; Jackson et al., 2020). Therefore, the "missing nitrogen" mystery still remains.

Iron nitrides are likely the main nitrogen-bearing species under reducing conditions in the deep Earth down to the core-mantle boundary (CMB) while NH_3 and NH_4^+ complexes are more abundant in shallow subduction zones (Huang et al., 2021; Speelmanns et al., 2018; Yoshioka et al., 2018). Naturally occurring iron nitrides have been frequently discovered, including orthorhombic Fe_2N and trigonal Fe_3N as inclusions in deep mantle diamonds from Rio Soriso, Brazil, and cubic Fe_4N (roaldite) in iron meteorites (Kaminsky & Wirth, 2017; Niellsen & Burhwald, 1981). The chemical and physical properties of these iron nitrides have been investigated at high P-T conditions (Kusakabe et al., 2019; Litasov et al., 2017; Lv et al., 2020; Minobe et al., 2015; Zhuang et al., 2021). Fe_7N_3 shows an identical structure to Fe_7C_3 which has been considered a potential candidate phase in the inner core (Chen et al., 2014), and its thermal stability and melting have been investigated to 135 GPa and 3,100 K (Kusakabe et al., 2019; Minobe et al., 2015). Other iron nitrides like hcp ζ-Fe_2N, nonstoichiometric ε-Fe_3Nx ($0.75 < x < 1.5$), and fcc γ'-Fe_4N have also been experimentally confirmed to be stable up to 40–70 GPa at room temperature, but their thermal stability has not been well studied yet (Litasov et al., 2017). Additionally, the iron spin transition, equation of state, and electrical conductivity of these nitrides have recently been studied (Huang et al., 2021; Lv et al., 2020; Zhang & Yin, 2012; Zhuang et al., 2021).

The melting behavior of iron nitrides at high pressure largely dictates the mobility and distribution of nitrogen in the deep mantle, and may contribute to the high C/N ratio in the BSE. However, the melting behavior of iron nitrides has not been thoroughly studied under mantle pressures. Among the known Fe–N intermediate compounds, only the melting curve of Fe_7N_3 was experimentally determined to lower mantle conditions (Kusakabe et al., 2019). The melting curves of other common iron nitrides including Fe_2N and Fe_3N are still unknown at high pressure. A battery of factors may influence the melting temperature of iron nitrides, including the iron spin transition, nitrogen concentration, and carbon incorporation. For instance, the phase transition from the high-spin (HS) to low-spin (LS) electronic state greatly depresses the melting curve of lower-mantle ferropericlase (Fu et al., 2018). The increasing concentrations of alloying C, S, and O reduce the melting temperature of iron-rich alloys (Morard et al., 2017). In brief, the high-pressure melting of iron nitrides is of the utmost importance for better understanding nitrogen circulations in the deep Earth and the 'missing nitrogen' mystery.

In this study, the melting behavior of Fe_2N, Fe_3N, Fe_7N_3, and Fe_3C was investigated systematically up to 80 GPa using laser-heated diamond anvil cells (LHDACs). The new melting diagnostics of highly sensitive electrical resistance jump was adopted to determine the onset of melting at high pressure. Additionally, it is for the first time in LHDACs that N_2 degassing was observed out of nitrogen-rich metallic liquids under low P and high T. These results establish an overall understanding of the high-P melting features of the Fe–N–C system, suggesting that low-P N_2 degassing and ultralow melting temperatures may help decipher the high C/N ratio of the BSE.

2. Materials and Methods

2.1. Starting Materials

Polycrystalline Fe_2N (99.9%) and Fe_3N (99.9%) samples were commercially purchased from the Beijing An-Teck company, while the Fe_7N_3 sample was synthesized from the mixture of Fe and NaN_3 at 5 GPa and 2073 K at the Center for High Pressure Science and Technology Advanced Research (HPSTAR). The Fe_3C sample was also prepared at HPSTAR using the same synthesis procedure as described in Liu et al. (2016). X-ray diffraction (XRD) experiments were performed on these samples to confirm their structure (Zhuang et al., 2021). High-P melting experiments were performed using LHDACs to determine the melting temperature of iron nitrides with

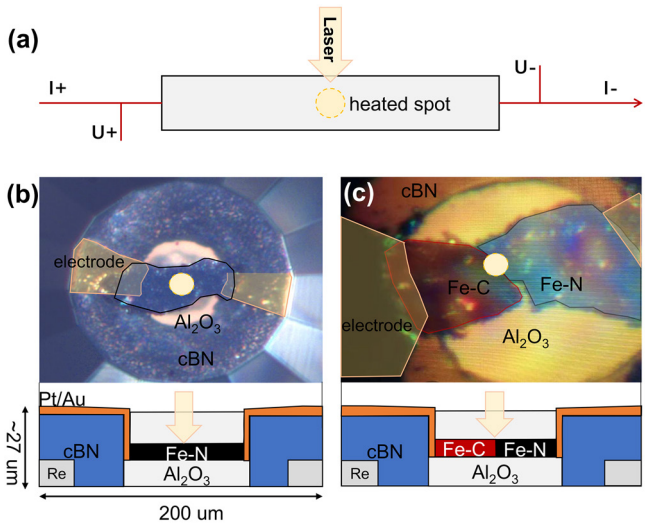

Figure 1. Experimental setup for high-pressure melting experiments. (a) A circuit diagram for electrical resistance measurements. A constant current of 10 mA is applied while the electric potential difference is recorded with increasing laser power. The resistance of sample is calculated via the Ohm's law. (b) A schematic diagram of the sample loading configuration for the Fe–N system from both top and vertical views. Rhenium (Re) is the outer gasket and a mixture of cubic boron nitride (cBN) and epoxy serves as the inner gasket and the insulation layer. (c) A schematic diagram of the sample loading configuration for the Fe–N–C system from both top and vertical views. The laser beam is focused on the junction area of the Fe–N and Fe–C samples.

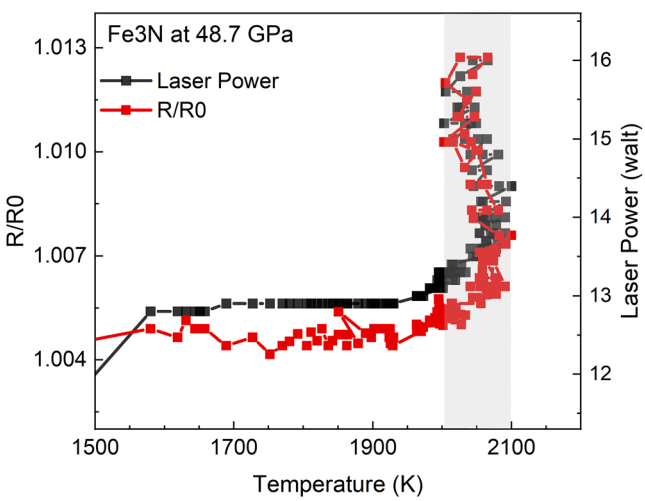

Figure 2. The R/R_0 ratio and laser power as a function of temperature for Fe_3N. The black line indicates the relation between laser power and temperature while the red line shows the relation of temperature and electrical resistance. R_0 is the resistance of the sample before heating and R is the timely resistance of the sample upon heating. Once the melting temperature is reached as shown in the shadow region, the resistance changes sharply. The melting temperature corresponds to the average temperature of the shadow region while standard deviation is considered the uncertainty of the temperature (comparable to the width of the shadow region).

the sensitive melting diagnostic of electrical resistance jump. In addition, High-*P* laser Raman spectroscopy measurements were conducted to track samples and run products before and after laser heating.

2.2. High-Pressure Melting of Iron Nitrides Explored by Electrical Resistance Jump

Melting experiments were performed on iron nitrides (Fe_2N, Fe_3N, and Fe_7N_3) in the LHDACs with a culet size of 200 μm. A hole of 4/5 culet size was drilled into the center of the pre-indented Re gasket. A powder mixture of cubic boron nitride (cBN) and epoxy was compacted into the hole, serving as an inner gasket and electrical insulation. Iron nitride samples were first packed into a 6–8 μm thick foil in thickness between a pair of diamond anvils with a culet size of 500 μm. Next, the iron nitride sample was cut into an 80–100 μm long and 25–30 μm wide strip. Then, the iron nitride sample was loaded into the LHDAC and further sandwiched between 2 and 10 μm-thick platelets of dry Al_2O_3 serving as both the pressure-transmitting medium and thermal insulation layers. Two Pt/Au foils were in contact with each side of the sample along the long direction of the sample, which served as electrodes (Figure 1). The whole setup was heated at 423 K for 4–12 hr in a vacuum drying oven to remove moisture before the LHDAC sample chamber was sealed.

Furthermore, high-pressure melting experiments were performed on the Fe–N–C system. We designed a new sample configuration for the Fe–N–C system in the LHDACs unlike the Fe-N system (Figure 1c). First, each Fe_7N_3 or Fe_3C sample was prepared into 3–4 μm thick, ~30 μm wide, and 50–80 μm long strips. Two strips of Fe_7N_3 and Fe_3C were then overlapped in the sample chamber. A laser beam was focused on the junction area to heat both Fe_7N_3 and Fe_3C concurrently. In particular, the Fe_7N_3 and Fe_3C strips themselves were used as electrodes contacting the Pt/Au foils at the edge of the diamond-anvils. In most of the high-pressure melting experiments, the electrical resistance change was monitored to detect the incipient melting of the Fe–N–C system, coupled with the conventional method of temperature plateau as a function of laser power.

An ytterbium CW fiber laser with a wavelength of 1,070 nm was adopted to heat the sample up on one side. The heating spot was about 30 μm in the FWHM and the signals emitted from the center 10 × 10 μm of the laser-heating spot were collected by using Acton SP-2156 spectrograph. The temperature was calibrated at 2,993 K using an Oriel NIST traceable calibrated quartz tungsten halogen lamp. The temperature was determined by fitting the spectrum between 600 and 800 nm to the Planck radiation function (Anzellini & Boccato, 2020). The temperature uncertainty mainly results from the temperature fluctuation upon the incipient melting and the fits to experimental data with the gray body radiation theory (approximately 5% of the measured temperature values) (Mori et al., 2017) (Figure 2). The pressure was measured with the Raman shift of the diamond culet tip directly on top of the laser-heating spot after melting experiments, and the pressure uncertainty was determined by multiple measurements on the laser heating spot. The thermal pressure was estimated following Zhang et al. (2016). Since the thermal EOS parameters of Fe_3N and Fe_2N were not available from previous studies, the thermal pressure contribution for iron nitrides was set to 5% per 1,000 K following Minobe et al. (2015).

The electrical resistance values of the iron nitrides and Fe–N–C mixtures were measured following Ohm's law. A constant current of 10 mA was supplied using a Keithley 2410 DC supplier, while the voltage across the sample was measured with a Keithley 6221 nanovoltmeter. The electrical resistance was recorded during laser heating with increasing laser power and the heating spot temperature was recorded simultaneously. The electrical resistance at room temperature before laser heating was defined as R_0, and the relation between the temperature (T) and high-temperature electrical resistance (R) can be obtained as the T–R/R_0. The melting temperature (T_m) was determined at the onset of a sharp change in the T–R/R_0 slope, where an obvious jump would be observed in the electrical resistance values.

2.3. High-Pressure Laser Raman Spectroscopic Measurements

The Fe_3N samples were pre-pressed to 7–10 μm thick before being loaded into LHDACs with a culet size of 250–300 μm. Ar was loaded using the high-pressure gas loading system at HPSTAR, to serve as a pressure-transmitting medium, while 5–10 μm diameter ruby spheres were adopted as pressure calibration. The pressure was determined from the ruby fluorescence before and after each heating cycle. The sample was heated with additional laser power by ~5 W on both sample sides for ~3 s to surpass the melting temperature. High-pressure laser Raman spectra of Fe_3N were collected at room temperature using a Renishaw RM1000 Raman microscope at HPSTAR. The green 532 nm wavelength laser was used to excite Raman signals with a power of 25 mW. The spectral resolution was about ±1 cm^{-1} with a holographic diffraction grating of 1,800 lines/mm. Raman spectra were collected at around 2,350 cm^{-1} in a scan map of 5 × 5 μm before and after each run of laser heating. Such a practice can greatly avoid the disturbance from both the fluorescence of the diamond anvil and N_2 in the air. The scan time was typically 90 s for each Raman spectrum.

3. Results and Discussion

3.1. Reliability of the High-Pressure Melting Criterion

The electrical resistance jump, together with the relationship between laser power and temperature, was used as the primary criterion to determine the onset of melting in this study (Figure 2). The resistance jump diagnostics is sensitive since the sample resistance changes immediately in response to a tiny portion of melt by <1–2 vol% in the sample (Hou et al., 2021). Previous studies on iron melting illustrated the advantage of resistance jump diagnostics, coupled with the high P-T techniques of diamond-anvil cell and resistive/laser heating (Basu et al., 2020; Hou et al., 2021; Ohta et al., 2016; Sinmyo et al., 2019). An explanation for the resistance increase during the onset of melting is that the loss of long-range order and positional disorder aggravates the scattering of the conduction electrons in metallic iron (Basu et al., 2020; Hou et al., 2021). In addition, the deformation of the partially molten sample and consequent changes in grain boundaries can further contribute to the resistance jump. On the contrary, certain disadvantages are involved with traditional melting diagnostics that have been adopted as the primary melting criteria of iron alloys under high pressures, such as melt flow, quench texture, temperature plateau with increasing laser power, diffuse scattering in XRD patterns, X-ray absorption spectroscopy, and synchrotron Mössbauer spectroscopy (Anzellini et al., 2013; Aquilanti et al., 2015; Boehler, 1993; Jackson et al., 2013; Murphy et al., 2011; Nguyen & Holmes, 2004; Shen et al., 1998; Sinmyo et al., 2019; Williams et al., 1991; Zhang et al., 2016). In general, these X-ray-based criteria need a certain fraction of liquid in the detected area while melts tend to flow out during laser heating; accordingly, the melting temperature may be overestimated based on X-ray probes (Hou et al., 2021; Sinmyo et al., 2019). Other criteria including melt flow and quench texture are inefficient or greatly dependent on personal judgment. Apart from melting criteria, the reliability of melting determination is also affected by the sample geometry, heating methods, possible chemical reactions, metrology, and the accuracy of pressure and temperature evaluation at high P-T conditions (Morard et al., 2018).

Furthermore, apart from high sensitivity, the electrical resistance jump criterion shows high reliability. The melting curve of Fe_7N_3 measured in this work agrees well with the previous study by Kusakabe et al. (2019) within uncertainty (Figure 3a). In the latter, the three methods including diffuse signal, temperature plateau with increasing laser power, and XRD peak intensity reduction were adopted jointly as the melting criteria (Kusakabe et al., 2019). The melting temperature values determined by the diffuse signal and temperature plateau with increasing laser power agree well with each other, but a large discrepancy exists with the XRD peak intensity

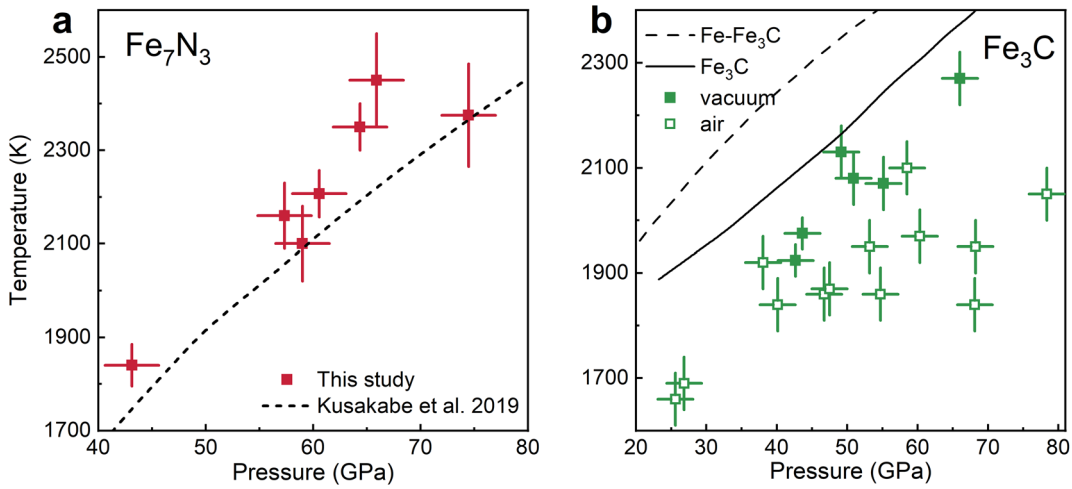

Figure 3. (a) Melting temperature of Fe_7N_3 at high pressure. Melting temperatures (red squares) are obtained based on the resistance jump criterion in this study. The melting curve of Fe_7N_3 (the dashed curve) reported by Kusakabe et al. (2019) was determined according to the diffuse signal, x-ray diffraction peak intensity reduction, and the discontinuity in laser power versus temperature relation. (b) Melting temperature of Fe_3C at high pressure. The resistance jump criterion is used in this study (the solid and open squares). The solid squares represent the solidus temperature of Fe_3C dehydrated in a vacuum drying oven at 423 K for 4–12 hr while the open squares are the solidus temperature of Fe_3C dehydrated in the air at 423 K for 3 hr. Dehydration in the air cannot remove all moisture, leading to the lower and divergent melting temperatures. The dashed line is the eutectic melting temperature of Fe-Fe_3C from Morard et al. (2017), and the solid line represents the melting temperature of Fe_3C from Liu et al. (2016). The intensity of the diffuse scattering was adopted as the primary melting criterion in these two studies.

reduction criterion. The phase transition of ε- to β-Fe_7N_3 at 40 GPa and 1,000 K could cause discontinuity in the high-pressure melting curve of Fe_7N_3. Therefore, the melting temperatures of Fe_7N_3 below 40 GPa were not discussed in this study with a focus on the high-pressure melting curve of β-Fe_7N_3. Moreover, high-pressure melting experiments were performed on Fe_3C with the resistance jump diagnostics. The solidus temperature of Fe_3C measured in this study is lower by 50–200 K than the previous work reported by Liu et al. (2016) (Figure 3b). It should be noted that the solidus temperature of Fe_3C from Liu et al. (2016) may be slightly overestimated since the integrated intensity of diffuse scattering signals from the liquid was used as the primary melting diagnostics. A certain amount of liquids at higher T, rather the onset of melting with lower T, is needed in these x-ray relevant criteria. In brief, the relatively consistent melting temperature between our results and the previous studies validates the reliability of the resistance jump criterion in this study.

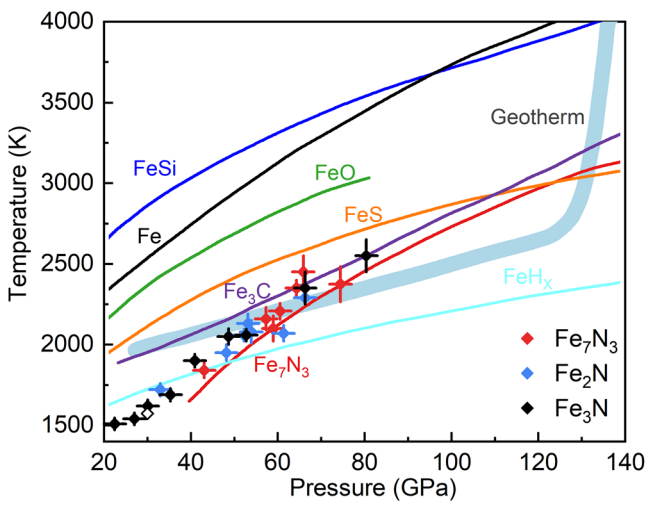

Figure 4. The melting curves of iron nitrides at high pressure. Black, blue, and red solid diamonds are the melting temperatures of: Fe_3N, Fe_2N, and Fe_7N_3, respectively, in this study. Open diamond: Fe_3N (Litasov et al., 2017). Red, blue, black, green, yellow, cyan, and purple lines are the melting curves of Fe_7N_3 (Kusakabe et al., 2019), FeSi (Lord et al., 2010), Fe (Anzellini et al., 2013; Hou et al., 2021), FeO (Fischer & Campbell, 2010), FeS (Boehler, 1992), FeH_x ($1 < x < 2$) (Hirose et al., 2019), and Fe_3C (Liu, Lin, et al., 2016), respectively. The shade area (light blue) is the present-day geotherm (Katsura et al., 2010).

3.2. High-Pressure Melting of Iron Nitrides

Melting temperatures were determined for iron nitrides (Fe_2N, Fe_3N, and Fe_7N_3) up to 80 GPa (Figure 4). In general, the melting temperatures of iron nitrides increase from 1,500 K, 20 GPa to 2,500 K, 80 GPa. The melting temperatures of all the three iron nitrides are comparable within uncertainties in temperature and linearly correlated with pressure. Therefore, all the melting temperature data could be fitted to the same Simon–Glatzel equation: $T = T_0[1 + (P - P_0)/a]^{1/c}$ with P_0 = 40 GPa (fixed), T_0 = 1,826 ± 13 K, a = 62 ± 13, and c = 1.5 ± 0.3 (Simon & Glatzel, 1929). The melting curve of the iron nitrides in this study is comparable to that of Fe_7N_3 reported by Kusakabe et al. (2019).

Our high-pressure melting experiments reveled the uncorrelation between nitrogen concentration and melting temperatures for iron nitrides. Similar

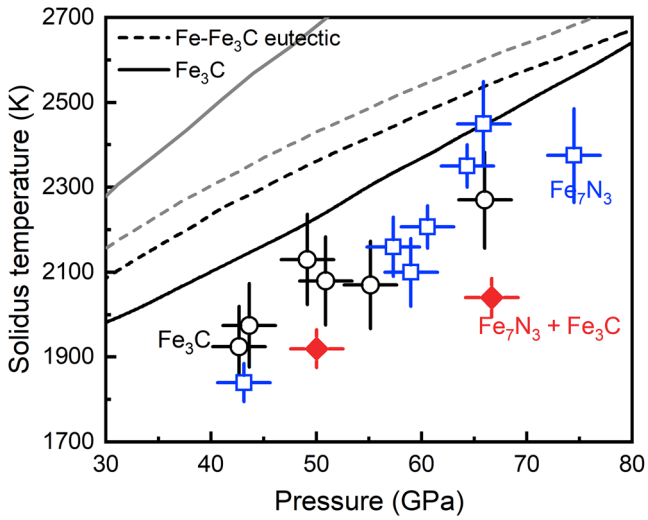

Figure 5. Melting temperature of Fe–C, Fe–N, and Fe–C–N systems under high pressure. Black circles and blue squares are the melting temperature of Fe_3C and Fe_7N_3, respectively. The red solid diamonds are the melting temperature of the compounds of Fe_3C and Fe_7N_3. The black and gray solid curves represent the solidus of Fe_3C at high pressure from Liu et al. (2016) and Takahashi et al. (2020), respectively. The black and gray dashed curve represent the eutectic melting of Fe–Fe_3C from Liu et al. (2016a) and Morard et al. (2017), respectively. Generally, the solidus data of Fe_3C obtained in this study is lower than those based on X-ray diagnostics, confirming the sensitivity of the resistance jump melting criterion. The discrepancies in the melting temperatures are marginal in the two studies of Fe–Fe_3C eutectic system. However, large discrepancies exist between the two studies on Fe_3C, which may result from the use of different melting diagnostics.

phenomena were also reported for the electrical and thermal conductivity of iron nitrides, which are negligibly affected by nitrogen concentration under high pressures (Zhuang et al., 2021). This is related to similar atomic structures of iron nitrides, where iron atoms are close-packed while octahedral sites are occupied by nitrogen atoms. However, the phase diagram of the Fe–N binary system has not been well investigated under high pressures (Göhring et al., 2016). Therefore, it remains an open question whether other Fe–N compounds with much lower or higher nitrogen concentrations have comparable melting temperatures.

The eutectic melting temperature of the Fe–N system is ~1,580 K with a nitrogen content of ~3–4 wt.% at ambient pressure (Du, 2007). However, neither the eutectic composition nor eutectic melting temperature under high pressures has been investigated yet. Considering the similarity in geochemical properties of carbon and nitrogen, it is beneficial to compare the high-pressure melting behavior between the Fe–N and Fe–C systems (Huang et al., 2021; Sagatov et al., 2019). Although it remains controversial for the eutectic composition of 1.5 or 3.0 wt.% C in the Fe–C system, high *P-T* experiments reached almost the same melting temperatures (Fei & Brosh, 2014; Liu, Li, et al., 2016; Lord et al., 2009; Morard et al., 2017). In particular, the melting curves of Fe_3C and the Fe-C eutectic system are indistinguishable within temperature uncertainties (Figure 5) (Liu, Li, et al., 2016; Liu, Lin, et al., 2016). By analogy to Fe–C system, it could be inferred that the eutectic melting temperature of Fe-N system may like those of iron nitrides under high pressures.

3.3. Melting of the Fe–N–C System

Nitrogen is likely to exist in iron carbonitrides and nitrides in the deep mantle (Kaminsky & Wirth, 2017; Marty, 2012; Sokol et al., 2017). It is thus necessary to know how the melting behavior of the Fe–N system changes in the presence of carbon. The melting temperatures of the Fe_3C-Fe_7N_3 mixture were measured between 40 and 70 GPa (Figure 5). A weak reduction was observed in the Fe-N-C system with respect to the melting temperatures of Fe_3C and Fe_7N_3 under high pressures. Moreover, previous thermodynamic simulations predicated the addition of 0.5 wt.% carbon would not noticeably reduce the melting temperature of the Fe–N system at ambient pressure (Du, 2007). Later, high *P-T* experiments on the Fe-Fe_3C-Fe_3N system suggested that nitrogen solubility in Fe_3C is limited to 0.5 wt.% up to 7.8 GPa and 1,623 K, while considerable carbon could be dissolved in Fe_3N (Sokol et al., 2017). The subsolidus phase sequences with increasing nitrogen are γ-Fe→γ-Fe + Fe_3N→Fe_3N and Fe_3C→Fe_3C + Fe_3N→Fe_3N for the Fe–N and Fe–N–C systems, respectively. However, the difference in the melting curves between the Fe–N and Fe–N–C systems has not been studied yet. Some clues could be derived from other Fe–X–Y ternary systems, such as $Fe_{97.53}Si_{1.57}C_{0.90}$ and $Fe_{90}O_8S_2$ (the subscript values in the unit of wt.%) (Huang et al., 2010; Miozzi et al., 2020). The melting curve of $Fe_{97.53}Si_{1.57}C_{0.90}$ is comparable to that of $FeC_{1.5}$, but much lower than that of the Fe-Si eutectic composition. The melting curve of $Fe_{90}O_8S_2$ is mostly comparable to that of FeS, but much lower than that of FeO under mantle pressures. In other words, the melting temperature of the Fe–X–Y ternary system is generally lower than that of both Fe–X and Fe–Y binary systems. In this study, the melting temperatures of the Fe–N–C system are mildly lower than both the Fe–N and Fe–C systems.

3.4. N_2 Degassing out of Molten Iron Nitride at Low Pressure

Raman signature of N≡N was observed in the quenched Fe_3N samples at pressures less than 12 GPa (Figure 6). It demonstrated the degassing of N_2 out of Fe_3N liquid at low *P* and high *T*. N_2 was no longer detected at pressures greater than 12 GPa, which can be ascribed to the increasing solubility of nitrogen in iron-rich liquids with increasing pressure (Speelmanns et al., 2018). Based on the model of nitrogen solubility in metallic melts as a function of pressure and temperature, the Fe_3N melt (with 7.7 wt.% N) would not degas under pressures above 8.5 GPa (Speelmanns et al., 2018). This discrepancy may be caused by different oxygen fugacity between LHDAC and

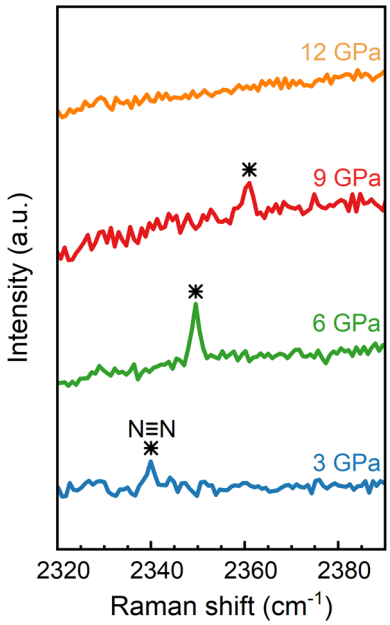

Figure 6. Representative Raman spectra of N_2 degassing from Fe_3N at high *P-T* conditions. Spectra are obtained on quenched samples after heating up to ~2,000 K. The asterisks indicate the peak of N≡N. No more N_2 is degassed out from Fe_3N melts at higher pressure due to the increasing nitrogen solubility in iron-rich melt with increasing pressure.

multi-anvil experiments. Alternatively, a small amount of carbon might have diffused into the Fe-N melts from the diamond anvils during laser heating, which might decrease the solubility of nitrogen in iron-rich metallic liquids.

Furthermore, the immiscible nitrogen-rich liquid was reported in the Fe–C–N liquids (Liu et al., 2019). The solubility of nitrogen in metallic melts is controlled by *P*, *T*, and alloying composition (Speelmanns et al., 2018). In detail, the increasing pressure elevates the solubility of nitrogen in iron-rich metallic liquids, while the effect of increasing temperature is slightly negative. Silicon and carbon occupy the same interstices as nitrogen in iron-rich liquids; subsequently, Si and C perform as competitors and their presence would lower the solubility of nitrogen (Speelmanns et al., 2018; Stein & Hucklenbroich, 2004). On the contrary, sulfur hardly affects the solubility of nitrogen and the effect of coexisting oxygen is still controversial (Libourel et al., 2003; Speelmanns et al., 2018). Interestingly, the presence of sulfur can greatly minimize the solubility of carbon in iron-rich metallic liquids (Tsuno & Dasgupta, 2015).

4. Implications

N–H species have long been considered the predominant reservoir of nitrogen in the mantle (Mysen, 2019; Sokol et al., 2020). However, the present Earth's mantle is under relatively reduced conditions with 0.1–1 wt.% Fe alloys saturated below ~250 km that could react with N–H species to form iron nitrides and carbonitrides (Frost et al., 2004; Rohrbach et al., 2011). Given the moderately siderophile nature of nitrogen under mantle *P-T* conditions, a large portion of nitrogen may exist in the form of iron nitrides in the BSE, as evidenced by the observation of iron nitrides and carbonitrides inclusions in deep diamonds (Kaminsky & Wirth, 2017). In this study, the ultralow melting temperatures of the Fe–N–C system and low-pressure N_2 degassing of iron nitride liquids can be integrated to shed light on the redistribution and cycling of deep nitrogen and carbon through geologic time.

The presence of roaldite (Fe_4N) in taenite implies that nitrogen is heterogeneously distributed and locally saturated in some iron meteorites (Sugiura, 1998). However, the nitrogen concentration of the BSE is relatively lower with respect to chondrites. Degassing of iron nitrides from differentiated impactors plays an important role in nitrogen accretion on Earth. During impact events, the collision heat could be able to melt iron nitrides in meteorites, as well as form local or even global magma oceans. The metallic core of small impactors could be emulsified and iron nitrides or nitrogen-saturated iron alloys therein likely underwent N_2 degassing at shallow depths (Nimmo & Kleine, 2015). The coexistence of carbon, silicon, and nickel in Fe-rich melts might further reduce the nitrogen solubility and promote N_2 degassing upon impacts (Liu et al., 2019; Speelmanns et al., 2018). It is noted that the metallic cores of large impactors may merge into the core of the proto-Earth rapidly without metal-silicate chemical equilibrium, which could not decrease the N content in the primitive mantle.

Interestingly, the ultralow melting temperatures imply that iron nitrides are molten at depths of <1500 km in the mantle according to the present-day geotherm (Katsura et al., 2010). This controls the distribution and cycling of nitrogen in the BSE. Nitrogen should be largely hosted in the form of ammonium (NH_4^+) in the oxidized crust and upper mantle, whereas iron nitrides and carbonitrides could become major hosts for deep nitrogen in the mantle transition zone and the lower mantle due to the oxygen fugacity decreasing with depth (Frost & McCammon, 2008). Considering the limited metal content in the mantle and its high dihedral angle, neither percolation, diapirs nor melt-filled cracks would be active for the descending molten iron nitrides (Mao & Mao, 2020; Rohrbach & Schmidt, 2011; Shi et al., 2013; von Bargen & Waff, 1986). Alternatively, subducting slabs could provide a passage for isolated droplets of molten iron nitrides to sink to the lower mantle (Figure 7). Notably, nitrogen is less likely to be efficiently transported back to the shallow mantle via mantle plumes because iron nitrides would re-melt at depths of <1,500 km. The low-melting behavior of iron nitrides may lead to a nitrogen-depleted upper mantle, together with a nitrogen-enriched lower mantle. This mechanism may be not

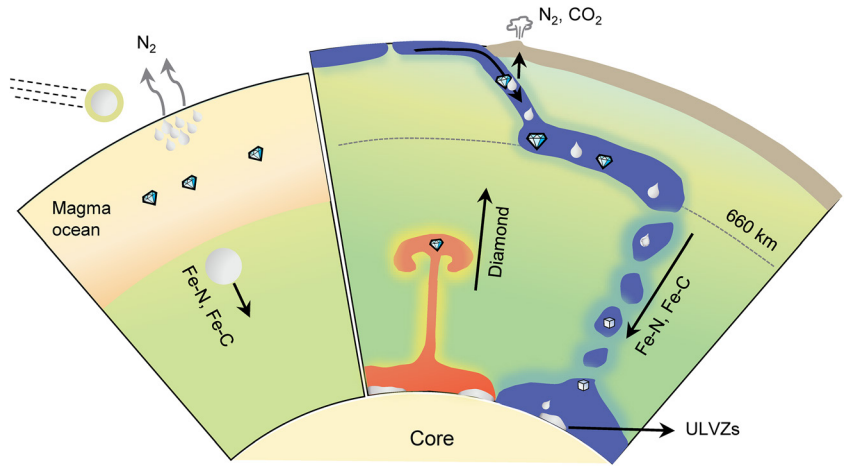

Figure 7. Schematic diagram of the two-stage model. The left part shows the first stage when impact events take place. Considerable N_2 is released from heated iron nitrides while carbon is hosted in diamond in the mantle. The right part shows the second stage when mantle cycle takes place. Apart from the shallow circulation of nitrogen and carbon in the subduction zones. Considerable carbon is transferred upwards to the upper mantle while nitrogen exists in Fe–N system which cannot be easily transferred upwards due to the high density. The light drops and cubes indicate that nitrogen existing in liquid and solid phases, respectively.

applicable to deep carbon cycling in the mantle due to the higher melting temperature of iron carbides (Liu, Li, et al., 2016) and the enhanced mobility of carbon as a result of redox melting and freezing of mantle carbon (Fei & Stagno, 2020; Rohrbach & Schmidt, 2011). The difference of melting temperatures between Fe–N and Fe–C systems alters the cycling paths of deep nitrogen and carbon, resulting in heterogeneous distribution of carbon and nitrogen throughout the mantle.

5. Conclusions

The novel resistance jump criterion was used to investigate the melting behavior of iron nitrides and the Fe–N–C system under high pressures. The melting curves of Fe_2N, Fe_3N, and Fe_7N_3 are comparable and almost linearly correlated to pressure at 20–80 GPa. Nitrogen concentration seems to barely affect the high-pressure melting curves of iron nitrides. The ultralow melting temperatures of iron nitrides indicate that subducting nitrogen could be transported downwards and accumulate in the lower mantle. On the other hand, N_2 could be separated from iron nitride melts at relatively lower pressures (<12 GPa for Fe_3N liquid). The low melting temperature of iron nitrides at 20–80 GPa, together with the N_2 degassing of Fe–N melts at lower pressures, could play important roles in the accretion, distribution, and cycling of nitrogen on Earth through time and space.

Data Availability Statement

Datasets for the high-pressure experimental measurements are available at the link (https://zenodo.org/record/5206109).

Acknowledgments
We thank Liangxu Xu and Xueyan Du for their experimental assistance and Xiaokang Feng for providing the Fe_7N_3 sample. This work is supported by the National Natural Science Foundation of China (NSFC Grant Nos. 42072052 and U1930401). Some experiments are supported by the Synergic Extreme Condition User Facility (SECUF) and BL15U at the Shanghai Synchrotron Radiation Facility (SSRF).

References

Adler, J. F., & Williams, Q. (2005). A high-pressure X-ray diffraction study of iron nitrides: Implications for Earth's core. *Journal of Geophysical Research*, *110*(B1), B01203. https://doi.org/10.1029/2004jb003103

Alexander, C. M. D., Howard, K. T., Bowden, R., & Fogel, M. L. (2013). The classification of CM and CR chondrites using bulk H, C and N abundances and isotopic compositions. *Geochimica et Cosmochimica Acta*, *123*, 244–260. https://doi.org/10.1016/j.gca.2013.05.019

Anzellini, S., & Boccato, S. (2020). A practical review of the Laser-heated diamond anvil cell for university laboratories and synchrotron applications. *Crystals*, *10*(6459), 459. https://doi.org/10.3390/cryst10060459

Anzellini, S., Dewaele, A., Mezouar, M., Loubeyre, P., & Morard, G. (2013). Melting of iron at Earth's inner core boundary based on fast X-ray diffraction. *Science*, *340*(6131), 464–466. https://doi.org/10.1126/science.1233514

Aquilanti, G., Trapananti, A., Karandikar, A., Kantor, I., Marini, C., Mathon, O., et al. (2015). Melting of iron determined by X-ray absorption spectroscopy to 100 GPa. *Proceedings of the National Academy of Sciences*, *112*(39), 12042–12045. https://doi.org/10.1073/pnas.1502363112

Basu, A., Field, M. R., McCulloch, D. G., & Boehler, R. (2020). New measurement of melting and thermal conductivity of iron close to outer core conditions. *Geoscience Frontiers*, *11*(2), 565–568. https://doi.org/10.1016/j.gsf.2019.06.007

Bergin, E. A., Blake, G. A., Ciesla, F., Hirschmann, M. M., & Li, J. (2015). Tracing the ingredients for a habitable earth from interstellar space through planet formation. *Proceedings of the National Academy of Sciences*, *112*(29), 8965–8970. https://doi.org/10.1073/pnas.1500954112

Boehler, R. (1992). Melting of the Fe-FeO and the Fe-FeS systems at high pressure: Constraints on core temperatures. *Earth and Planetary Science Letters*, *111*(2–4), 217–227. https://doi.org/10.1016/0012-821X(92)90180-4

Boehler, R. (1993). Temperatures in the Earth's core from melting-point measurements of iron at high static pressures. *Nature*, *363*(6429), 534–536. https://doi.org/10.1038/363534a0

Chen, B., Li, Z., Zhang, D., Liu, J., Hu, Y. M., Zhao, J., et al. (2014). Hidden carbon in Earth's inner core revealed by shear softening in dense Fe_7C_3. *Proceedings of the National Academy of Sciences*, *111*(50), 17755–17758. https://doi.org/10.1073/pnas.1411154111

Dalou, C., Furi, E., Deligny, C., Piani, L., Caumon, M.-C., Laumonier, M., et al. (2019). Redox control on nitrogen isotope fractionation during planetary core formation. *Proceedings of the National Academy of Sciences*, *116*(29), 14485–14494. https://doi.org/10.1073/pnas.1820719116

Dalou, C., Hirschmann, M. M., von der Handt, A., Mosenfelder, J., & Armstrong, L. S. (2017). Nitrogen and carbon fractionation during core-mantle differentiation at shallow depth. *Earth and Planetary Science Letters*, *458*, 141–151. https://doi.org/10.1016/j.epsl.2016.10.026

Dauphas, N. (2017). The isotopic nature of the Earth's accreting material through time. *Nature*, *541*(7638), 521–524. https://doi.org/10.1038/nature20830

Du, H. (2007). A reevaluation of the Fe-N and Fe-C-N systems. *Journal of Phase Equilibria*, *14*(6), 682–693. https://doi.org/10.1007/bf02667880

Fei, Y., & Brosh, E. (2014). Experimental study and thermodynamic calculations of phase relations in the Fe–C system at high pressure. *Earth and Planetary Science Letters*, *408*, 155–162. https://doi.org/10.1016/j.epsl.2014.09.044

Fei, Y., & Stagno, V. (2020). The redox boundaries of Earth's interior. *Elements*, *16*(3), 167–172. https://doi.org/10.2138/gselements.16.3.167

Fischer, R. A., & Campbell, A. J. (2010). High-pressure melting of wustite. *American Mineralogist*, *95*(10), 1473–1477. https://doi.org/10.2138/am.2010.3463

Frost, D. J., Liebske, C., Langenhorst, F., McCammon, C. A., Tronnes, R. G., & Rubie, D. C. (2004). Experimental evidence for the existence of iron-rich metal in the Earth's lower mantle. *Nature*, *428*(6981), 409–412. https://doi.org/10.1038/nature02413

Frost, D. J., & McCammon, C. A. (2008). The redox state of Earth's mantle. *Annual Review of Earth and Planetary Sciences*, *36*(1), 389–420. https://doi.org/10.1146/annurev.earth.36.031207.124322

Fu, S., Yang, J., Zhang, Y., Liu, J., Greenberg, E., Prakapenka, V. B., et al. (2018). Melting behavior of the lower-mantle ferropericlase across the spin crossover: Implication for the ultra-low velocity zones at the lowermost mantle. *Earth and Planetary Science Letters*, *503*, 1–9. https://doi.org/10.1016/j.epsl.2018.09.014

Göhring, H., Fabrichnaya, O., Leineweber, A., & Mittemeijer, E. J. (2016). Thermodynamics of the Fe-N and Fe-N-C systems: The Fe-N and Fe-N-C phase diagrams revisited. *Metallurgical and Materials Transactions A*, *47*(12), 6173–6186. https://doi.org/10.1007/s11661-016-3731-0

Goldblatt, C., Claire, M. W., Lenton, T. M., Matthews, A. J., Watson, A. J., & Zahnle, K. J. (2009). Nitrogen-enhanced greenhouse warming on early Earth. *Nature Geoscience*, *2*(12), 891–896. https://doi.org/10.1038/ngeo692

Grady, M. M., & Wright, I. P. (2003). Elemental and isotopic abundances of carbon and nitrogen in meteorites. *Space Science Reviews*, *106*(1), 231–248. https://doi.org/10.1023/A:1024645906350

Grewal, D. S., Dasgupta, R., Holmes, A. K., Costin, G., Li, Y., & Tsuno, K. (2019). The fate of nitrogen during core-mantle separation on Earth. *Geochimica et Cosmochimica Acta*, *251*, 87–115. https://doi.org/10.1016/j.gca.2019.02.009

Hirose, K., Tagawa, S., Kuwayama, Y., Sinmyo, R., Morard, G., Ohishi, Y., & Genda, H. (2019). Hydrogen limits carbon in liquid iron. *Geophysical Research Letters*, *46*(10), 5190–5197. https://doi.org/10.1029/2019gl082591

Hirschmann, M. M. (2016). Constraints on the early delivery and fractionation of Earth's major volatiles from C/H, C/N, and C/S ratios. *American Mineralogist*, *101*(3), 540–553. https://doi.org/10.2138/am-2016-5452

Hou, M., Liu, J., Zhang, Y., Du, X., Dong, H., Yan, L., et al. (2021). Melting of iron explored by electrical resistance jump up to 135 GPa. *Geophysical Research Letters*, *48*(20), 095739. https://doi.org/10.1029/2021GL095739

Huang, H., Hu, X., Jing, F., Cai, L., Shen, Q., Gong, Z., & Liu, H. (2010). Melting behavior of Fe-O-S at high pressure: A discussion on the melting depression induced by O and S. *Journal of Geophysical Research*, *115*(B5), B05207. https://doi.org/10.1029/2009jb006514

Huang, S., Wu, X., Zhu, F., Lai, X., Li, J., Neill, O. K., et al. (2021). High-pressure phase stability and thermoelastic properties of iron carbonitrides and nitrogen in the deep Earth. *Journal of Geophysical Research: Solid Earth*, *126*(6), B021934. https://doi.org/10.1029/2021jb021934

Jackson, C., Cottrell, E., Du, Z., Bennett, N., & Fei, Y. (2020). *Core formation and magma ocean outgassing set planetary N-S-C ratios*. https://doi.org/10.21203/rs.3.rs-40405/v1

Jackson, J. M., Sturhahn, W., Lerche, M., Zhao, J., Toellner, T. S., Alp, E. E., et al. (2013). Melting of compressed iron by monitoring atomic dynamics. *Earth and Planetary Science Letters*, *362*, 143–150. https://doi.org/10.1016/j.epsl.2012.11.048

Jacobs, H., Rechenbach, D., & Zachwieja, U. (1995). Structure determination of γ′-Fe4N and ϵ-Fe3N. *Journal of Alloys and Compounds*, *227*(1), 10–17. https://doi.org/10.1016/0925-8388(95)01610-4

Kaminsky, F., & Wirth, R. (2017). Nitrides and carbonitrides from the lowermost mantle and their importance in the search for Earth's "lost" nitrogen. *American Mineralogist*, *102*(8), 1667–1676. https://doi.org/10.2138/am-2017-6101

Katsura, T., Yoneda, A., Yamazaki, D., Yoshino, T., & Ito, E. (2010). Adiabatic temperature profile in the mantle. *Physics of the Earth and Planetary Interiors*, *183*(1–2), 212–218. https://doi.org/10.1016/j.pepi.2010.07.001

Kusakabe, M., Hirose, K., Sinmyo, R., Kuwayama, Y., Ohishi, Y., & Helffrich, G. (2019). Melting curve and equation of state of β-Fe_7N_3: Nitrogen in the Core? *Journal of Geophysical Research: Solid Earth*, *124*(4), 3448–3457. https://doi.org/10.1029/2018jb015823

Li, Y., Marty, B., Shcheka, S., Zimmermann, L., & Keppler, H. (2016). Nitrogen isotope fractionation during terrestrial core-mantle separation. *Geochemical Perspectives Letters*, *2*, 138–147. https://doi.org/10.7185/geochemlet.1614

Libourel, G., Marty, B., & Humbert, F. (2003). Nitrogen solubility in basaltic melt. Part I. Effect of oxygen fugacity. *Geochimica et Cosmochimica Acta*, *67*(21), 4123–4135. https://doi.org/10.1016/s0016-7037(03)00259-x

Litasov, K. D., Shatskiy, A., Ponomarev, D. S., & Gavryushkin, P. N. (2017). Equations of state of iron nitrides ε-Fe_3N_x and γ-Fe_4N_y to 30 GPa and 1200 K and implication for nitrogen in the Earth's core. *Journal of Geophysical Research: Solid Earth*, *122*(5), 3574–3584. https://doi.org/10.1002/2017jb014059

Liu, J., Dorfman, S. M., Lv, M., Li, J., Zhu, F., & Kono, Y. (2019). Loss of immiscible nitrogen from metallic melt explains Earth's missing nitrogen. *Geochemical Perspectives Letters*, 18–22. https://doi.org/10.7185/geochemlet.1919

Liu, J., Li, J., Hrubiak, R., & Smith, J. S. (2016). Origins of ultralow velocity zones through slab-derived metallic melt. *Proceedings of the National Academy of Sciences*, *113*(20), 5547–5551. https://doi.org/10.1073/pnas.1519540113

Liu, J., Lin, J. F., Prakapenka, V. B., Prescher, C., & Yoshino, T. (2016). Phase relations of Fe_3C and Fe_7C_3 up to 185 GPa and 5200 K: Implication for the stability of iron carbide in the Earth's core. *Geophysical Research Letters*, *43*(2412), 12415–12444. https://doi.org/10.1002/2016GL071353

Lord, O. T., Walter, M. J., Dasgupta, R., Walker, D., & Clark, S. M. (2009). Melting in the Fe–C system to 70 GPa. *Earth and Planetary Science Letters*, *284*(1–2), 157–167. https://doi.org/10.1016/j.epsl.2009.04.017

Lord, O. T., Walter, M. J., Dobson, D. P., Armstrong, L., Clark, S. M., & Kleppe, A. (2010). The FeSi phase diagram to 150 GPa. *Journal of Geophysical Research*, *115*(B6), B06208. https://doi.org/10.1029/2009jb006528

Lv, M., Liu, J., Zhu, F., Li, J., Zhang, D., Xiao, Y., & Dorfman, S. M. (2020). Spin transitions and compressibility of ε-Fe_7N_3 and γ′-Fe_4N: Implications for iron alloys in terrestrial planet cores. *Journal of Geophysical Research: Solid Earth*, *125*(11), B020660. https://doi.org/10.1029/2020jb020660

Mao, H.-k., & Mao, W. L. (2020). Key problems of the four-dimensional Earth system. *Matter and Radiation at Extremes*, *5*(3), 038102. https://doi.org/10.1063/1.5139023

Marty, B. (2012). The origins and concentrations of water, carbon, nitrogen and noble gases on Earth. *Earth and Planetary Science Letters*, *313–314*, 56–66. https://doi.org/10.1016/j.epsl.2011.10.040

Minobe, S., Nakajima, Y., Hirose, K., & Ohishi, Y. (2015). Stability and compressibility of a new iron-nitride β-Fe_7N_3 to core pressures. *Geophysical Research Letters*, *42*(13), 5206–5211. https://doi.org/10.1002/2015gl064496

Miozzi, F., Morard, G., Antonangeli, D., Baron, M. A., Boccato, S., Pakhomova, A., et al. (2020). Eutectic melting of Fe-3 at% Si-4 at% C up to 200 GPa and implications for the Earth's core. *Earth and Planetary Science Letters*, *544*, 116382. https://doi.org/10.1016/j.epsl.2020.116382

Morard, G., Andrault, D., Antonangeli, D., Nakajima, Y., Auzende, A. L., Boulard, E., et al. (2017). Fe–FeO and Fe–Fe_3C melting relations at Earth's core–mantle boundary conditions: Implications for a volatile-rich or oxygen-rich core. *Earth and Planetary Science Letters*, *473*, 94–103. https://doi.org/10.1016/j.epsl.2017.05.024

Morard, G., Boccato, S., Rosa, A. D., Anzellini, S., Miozzi, F., Henry, L., et al. (2018). Solving controversies on the iron phase diagram under high pressure. *Geophysical Research Letters*, *45*(20). https://doi.org/10.1029/2018gl079950

Mori, Y., Ozawa, H., Hirose, K., Sinmyo, R., Tateno, S., Morard, G., & Ohishi, Y. (2017). Melting experiments on Fe–Fe_3S system to 254 GPa. *Earth and Planetary Science Letters*, *464*, 135–141. https://doi.org/10.1016/j.epsl.2017.02.021

Murphy, C. A., Jackson, J. M., Sturhahn, W., & Chen, B. (2011). Melting and thermal pressure of hcp-Fe from the phonon density of states. *Physics of the Earth and Planetary Interiors*, *188*(1–2), 114–120. https://doi.org/10.1016/j.pepi.2011.07.001

Mysen, B. (2019). Nitrogen in the earth: Abundance and transport. *Progress in Earth and Planetary Science*, *6*(1), 38. https://doi.org/10.1186/s40645-019-0286-x

Nguyen, J. H., & Holmes, N. C. (2004). Melting of iron at the physical conditions of the Earth's core. *Nature*, *427*(6972), 339–342. https://doi.org/10.1038/nature02248

Niellsen, H. P., & Burhwald, V. F. (1981). *Roaldite, a new nitride in iron meteorites. Paper presented at proceedings Lunar and planet science conference*.

Nimmo, F., & Kleine, T. (2015). Early differentiation and core formation: Processes and timescales. In J. Badro, & M. Walter (Eds.), *The early Earth: Accretion and differentiation* (pp. 83–102). Wiley. https://doi.org/10.1002/9781118860359.ch5

Ohta, K., Kuwayama, Y., Hirose, K., Shimizu, K., & Ohishi, Y. (2016). Experimental determination of the electrical resistivity of iron at Earth's core conditions. *Nature*, *534*(7605), 95–98. https://doi.org/10.1038/nature17957

Parvathi, V., Sofia, U., Murthy, J., & Babu, B. (2012). Probing the role of carbon in ultraviolet extinction along galactic sight lines. *The Astrophysical Journal*, *760*(1), 36. https://doi.org/10.1088/0004-637X/760/1/36

Rohrbach, A., Ballhaus, C., Ulmer, P., Golla-Schindler, U., & Schönbohm, D. (2011). Experimental evidence for a reduced metal-saturated upper mantle. *Journal of Petrology*, *52*(4), 717–731. https://doi.org/10.1093/petrology/egq101

Rohrbach, A., & Schmidt, M. W. (2011). Redox freezing and melting in the Earth's deep mantle resulting from carbon-iron redox coupling. *Nature*, *472*(7342), 209–212. https://doi.org/10.1038/nature09899

Sagatov, N., Gavryushkin, P. N., Inerbaev, T. M., & Litasov, K. D. (2019). New high-pressure phases of Fe7N3 and Fe7C3 stable at Earth's core conditions: Evidences for carbon–nitrogen isomorphism in Fe-compounds. *RSC Advances*, *9*(7), 3577–3581. https://doi.org/10.1039/c8ra09942a

Sakuraba, H., Kurokawa, H., Genda, H., & Ohta, K. (2021). Numerous chondritic impactors and oxidized magma ocean set Earth's volatile depletion. *Scientific Reports*, *11*(1), 20894. https://doi.org/10.1038/s41598-021-99240-w

Schlichting, H. E., & Mukhopadhyay, S. (2018). Atmosphere impact losses. *Space Science Reviews*, *214*(1), 34. https://doi.org/10.1007/s11214-018-0471-z

Shen, G., Mao, H. k., Hemley, R. J., Duffy, T. S., & Rivers, M. L. (1998). Melting and crystal structure of iron at high pressures and temperatures. *Geophysical Research Letters*, *25*(3), 373–376. https://doi.org/10.1029/97GL03776

Shi, C. Y., Zhang, L., Yang, W., Liu, Y., Wang, J., Meng, Y., et al. (2013). Formation of an interconnected network of iron melt at Earth's lower mantle conditions. *Nature Geoscience*, *6*(11), 971–975. https://doi.org/10.1038/ngeo1956

Simon, F., & Glatzel, G. (1929). Bemerkungen zur schmelzdruckkurve. *Zeitschrift fur Anorganische und Allgemeine Chemie*, *178*(1), 309–316. https://doi.org/10.1002/zaac.19291780123

Sinmyo, R., Hirose, K., & Ohishi, Y. (2019). Melting curve of iron to 290 GPa determined in a resistance-heated diamond-anvil cell. *Earth and Planetary Science Letters*, *510*, 45–52. https://doi.org/10.1016/j.epsl.2019.01.006

Sokol, A. G., Kruk, A. N., Seryotkin, Y. V., Korablin, A. A., & Palyanov, Y. N. (2017). Phase relations in the Fe-Fe3C-Fe3N system at 7.8 GPa and 1350°C: Implications for carbon and nitrogen hosts in Fe0-saturated upper mantle. *Physics of the Earth and Planetary Interiors*, *265*, 43–53. https://doi.org/10.1016/j.pepi.2017.02.007

Sokol, A. G., Kupriyanov, I. N., Seryotkin, Y. V., Sokol, E. V., Kruk, A. N., Tomilenko, A. A., et al. (2020). Cymrite as mineral clathrate: An overlooked redox insensitive transporter of nitrogen in the mantle. *Gondwana Research*, *79*, 70–86. https://doi.org/10.1016/j.gr.2019.08.013

Speelmanns, I. M., Schmidt, M. W., & Liebske, C. (2018). Nitrogen solubility in core materials. *Geophysical Research Letters*, *45*(15), 7434–7443. https://doi.org/10.1029/2018gl079130

Speelmanns, I. M., Schmidt, M. W., & Liebske, C. (2019). The almost lithophile character of nitrogen during core formation. *Earth and Planetary Science Letters*, *510*, 186–197. https://doi.org/10.1016/j.epsl.2019.01.004

Stein, G., & Hucklenbroich, I. (2004). Manufacturing and applications of high nitrogen steels. *Materials and Manufacturing Processes*, *19*(1), 7–17. https://doi.org/10.1081/AMP-120027494

Sugiura, N. (1998). Ion probe measurements of carbon and nitrogen in iron meteorites. *Meteoritics & Planetary Science*, *33*(3), 393–409. https://doi.org/10.1111/j.1945-5100.1998.tb01645.x

Takahashi, S., Ohtani, E., Sakai, T., Kamada, S., Ozawa, S., Sakamaki, T., et al. (2020). Phase and melting relations of Fe 3 C to 300 GPa and carbon in the core. In C. E. Manning, J.-F. Lin, & W. L. Mao (Eds.), *Phase and melting relations of Fe3C to 300 GPa and carbon in the core carbon in Earth's interior* (pp. 25–36). AGU. https://doi.org/10.1002/9781119508229.ch3

Tsuno, K., & Dasgupta, R. (2015). Fe–Ni–Cu–C–S phase relations at high pressures and temperatures – The role of sulfur in carbon storage and diamond stability at mid- to deep-upper mantle. *Earth and Planetary Science Letters*, *412*, 132–142. https://doi.org/10.1016/j.epsl.2014.12.018

Tucker, J. M., & Mukhopadhyay, S. (2014). Evidence for multiple magma ocean outgassing and atmospheric loss episodes from mantle noble gases. *Earth and Planetary Science Letters*, *393*, 254–265. https://doi.org/10.1016/j.epsl.2014.02.050

von Bargen, N., & Waff, H. S. (1986). Permeabilities, interfacial areas and curvatures of partially molten systems: Results of numerical computations of equilibrium microstructures. *Journal of Geophysical Research: Solid Earth*, *91*(B9), 9261–9276. https://doi.org/10.1029/JB091iB09p09261

Williams, Q., Knittle, E., & Jeanloz, R. (1991). The high-pressure melting curve of iron: A technical discussion. *Journal of Geophysical Research: Solid Earth*, *96*(B2), 2171–2184. https://doi.org/10.1029/90JB01999

Yoshioka, T., Wiedenbeck, M., Shcheka, S., & Keppler, H. (2018). Nitrogen solubility in the deep mantle and the origin of Earth's primordial nitrogen budget. *Earth and Planetary Science Letters*, *488*, 134–143. https://doi.org/10.1016/j.epsl.2018.02.021

Zhang, D., Jackson, J. M., Zhao, J., Sturhahn, W., Alp, E. E., Hu, M. Y., et al. (2016). Temperature of Earth's core constrained from melting of Fe and Fe0.9Ni0.1 at high pressures. *Earth and Planetary Science Letters*, *447*, 72–83. https://doi.org/10.1016/j.epsl.2016.04.026

Zhang, Y., & Yin, Q. (2012). Carbon and other light element contents in the Earth's core based on first-principles molecular dynamics. *Proceedings of the National Academy of Sciences*, *109*(48), 19579–19583. https://doi.org/10.1073/pnas.1203826109

Zhuang, Y., Su, X., Salke, N. P., Cui, Z., Hu, Q., Zhang, D., & Liu, J. (2021). The effect of nitrogen on the compressibility and conductivity of iron at high pressure. *Geoscience Frontiers*, *12*(2), 983–989. https://doi.org/10.1016/j.gsf.2020.04.012